Systematic Design Method and Experimental Validation of a 2-DOF Compliant Parallel Mechanism with Excellent Input and Output Decoupling Performances

Yao Jiang [1,2], Tiemin Li [2,3,*], Liping Wang [2,3] and Feifan Chen [1]

[1] Department of Precision Instrument, Institute of Instrument Science and Technology, Tsinghua University, Beijing 10084, China; jiangyao@mail.tsinghua.ed.cn (Y.J.); cff@mail.tsinghua.edu.cn (F.C.)
[2] Beijing Key Lab of Precision/Ultra-Precision Manufacturing, Equipments and Control, Tsinghua University, Beijing 100084, China; lpwang@mail.tsinghua.edu.cn
[3] Department of Mechanical Engineering, Institute of Manufacturing Engineering, Tsinghua University, Beijing 100084, China
* Correspondence: litm@tsinghua.edu.cn; Tel.: +86-010-6279-2792

Abstract: The output and input coupling characteristics of the compliant parallel mechanism (CPM) bring difficulty in the motion control and challenge its high performance and operational safety. This paper presents a systematic design method for a 2-degrees-of-freedom (DOFs) CPM with excellent decoupling performance. A symmetric kinematic structure can guarantee a CPM with a complete output decoupling characteristic; input coupling is reduced by resorting to a flexure-based decoupler. This work discusses the stiffness design requirement of the decoupler and proposes a compound flexure hinge as its basic structure. Analytical methods have been derived to assess the mechanical performances of the CPM in terms of input and output stiffness, motion stroke, input coupling degree, and natural frequency. The CPM's geometric parameters were optimized to minimize the input coupling while ensuring key performance indicators at the same time. The optimized CPM's performances were then evaluated by using a finite element analysis. Finally, a prototype was constructed and experimental validations were carried out to test the performance of the CPM and verify the effectiveness of the design method. The design procedure proposed in this paper is systematic and can be extended to design the CPMs with other types of motion.

Keywords: compliant mechanism; input and output decoupling; design method

1. Introduction

Manipulators with ultrahigh precision and resolution are urgently needed and play more and more important roles in modern technology, such as atomic force microscopy, ultra precision machining, biological cell manipulation, and chip assembly in the semiconductor industry [1–3]. However, conventional mechanisms make it difficult to meet these requirements due to their coarse accuracies caused by inevitable backlash, friction, and joint wear. By contrast, compliant mechanisms, which are composed of rigid links and flexure hinges, transmit motion solely through the deformation of materials. Therefore, they can provide high accuracy and resolution in micro-scale motion, benefitting from no friction, no backlash, no wear, and monolithic structure, while being easy to manufacture and assemble [4,5]. This kind of mechanism has already caught researcher's attention.

A typical compliant mechanism mainly consists of a mechanical structure with flexure members for motion transmission, piezoelectric elements for actuation, ultra-precision sensors for displacement output measurement, and controllers for motion control. Among them, the mechanical structure determines the performance of the compliant mechanism to a great extent. Two kinds of kinematic structures are commonly adopted, i.e., serial and parallel types [6]. Serial compliant mechanisms generally adopt a stack structure with one 1-DOF positioning stage mounted on another 1-DOF stage. This is a simple structure that is easy to manufacture and control, which has already been successfully applied in commercial products. However, it has the disadvantage of different dynamic characteristics of each axis, a reduced natural frequency as a result of the stacked stage increasing the moving mass, and cumulative motion errors [7]. The serial compliant stage will be suitable for applications where the motion along one axis is considerably faster than the others. Kenton [8] utilized a serial-kinematic nanopositioning stage for raster-type scanning, in which one axis is chosen for high-speed scanning while the other is designed for low-speed motion. Compared with the serial type, the parallel structure has inherent advantages in terms of high stiffness, large load capacity, low inertia, high natural frequency, and an absence of accumulation errors [9]. However, there have been many problems during the development of the parallel manipulator, particularly regarding conventional joints and rigid links. First, there are passive joints in the parallel manipulator, which are difficult to manufacture with high precision, such as sphere and universal joints. Meanwhile, the kinematic chains of the parallel manipulator are generally composed of elongated rods, which are prone to deformation and vibrate under external loads [10,11]. Because the displacement output of the terminal platform cannot be measured in real time to realize a closed-loop control, the above adverse factors will significantly decrease the motion accuracy of the parallel manipulator. Moreover, the kinematic model of parallel manipulator is complicated, which creates difficulties in kinematic calibration and motion control. The performance indicators, such as stiffness, dexterity, acceleration ability, will all change when the pose of the manipulator varies. Therefore, conventional parallel manipulators have not achieved their expected success in industry applications. Fortunately, the above issues will cease to be problems when the parallel structure is utilized in the development of a compliant mechanism. Apparently, there are no joints in the compliant parallel mechanism (CPM) and its displacement output can be measured directly as it relates to its micro motion stroke. Moreover, the pose of the CPM can be considered as a constant because its motion stroke is very small when compared to the geometric dimensions. This guarantees that the CPM can have a linear force–displacement relationship, identical mechanical bandwidth for each axis, and even decoupled kinematic model. Therefore, parallel structure has a great potential to be utilized in the development of a compliant mechanism, and numerous researchers have already begun working on it [12–15].

Though the CPM has advantages over its rigid counterpart, there are specific challenges in its design and development, which include the realization of cross-axis decoupling and actuation isolation [16–18], also known as output and input decoupling. Output coupling refers to any motion along one axis is affected by the actuation/input force along another axis. It results in a complicated kinematic model and additional calibration should be performed in the absence of terminal feedback. This is a typical character of a parallel manipulator due to its parallel kinematic type. The input coupling means that the input force on one actuation stage will cause the primary motion of another motion stage and thus bring additional loads on the actuator. Its effects can be neglected in a conventional parallel manipulator because the adopted motors have large stiffness and can bear any type of reacting force. For a CPM, however, the input coupling will cause unwanted deformations and even clearance between an actuator and the actuation point, which will result in difficulties to the motion control. Moreover, CPM adopts a piezoelectric actuator as its actuation element due to the actuator's high precision and resolution, large stiffness, high push force, and fast response. However, the piezoelectric actuator is made of multiple piezoelectric layers glued together and is thereby sensitive to pulling and bending forces that may damage the actuator. Therefore, the input coupling has adverse effects on the CPM and should be carefully considered in its design and development

process. Awtar [16,19] first proposed the decoupling performance design requirements of the parallel XY compliant mechanism. In order to realize actuation isolation, the actuator was required to be connected to the actuation point by means of a decoupler, which transmitted the axial force and absorbed any transverse motion without generating transverse loads. Lai [20] employed two types of distributed-compliance compound flexure modules and a mirror symmetric structure to reduce the input and output coupling of a novel 2-DOF compliant stage. Qin [21] utilized statically indeterminate symmetric structures to attenuate the cross-axis coupling of a proposed XY CPM. Li [22] investigated the design and development of a decoupled compliant stage with displacement amplifiers. The output decoupling was achieved by resorting to compound parallelogram flexures; the double compound parallelogram flexure and the amplifier acted as the decoupler to ensure this stage had excellent input decoupling characteristics.

There have already been several efficient and intuitive design approaches related to the compliant mechanisms, including the kinematic substitution method [20,23], constraint-based design method [24], and freedom and constraint topology [25,26]. However, these methods focus on the type synthesis and only guarantee the DOFs of the compliant mechanism instead of considering other performances. Additionally, they regard the degree and constrain of the compliant mechanism as those of the rigid mechanism. While the compliant mechanism moves through the deformations of materials, its DOFs are coupled with the stiffness property. Therefore, the type synthesis and structural design of the compliant mechanism are supposed to be integrated with the consideration of multiple performance indicators. The systematic design method for compliant mechanisms with excellent performances is still a great challenge. The practical CPMs are mostly directly provided in the present studies and there lacks a systematic process for guiding the design of a CPM with excellent decoupling performance. Considering the 2-DOF CPM [16–23,27–30] is the most practical compliant mechanism, this work's motivation is to present a systematic design of a decoupled 2-DOF CPM. The requirement on the kinematic structure for realizing totally output decoupling performance has been discussed. A flexure-based decoupler was chosen and its detail structure design was studied to minimize the input coupling of the CPM. Unlike the previous works, which only provided qualitative analyses, the specific definition and analytical model of the input coupling degree (ICD) of the CPM have been provided. According to the established model, the geometric parameters of the 2-DOF were optimized to directly minimize its ICD and the other key performance indicators were also guaranteed through constraint conditions. Finally, a prototype of the 2-DOF CPM was fabricated based on the optimized result, and several experimental tests were performed. A novel method was proposed within the tests, in order to evaluate the input coupling of the 2-DOF CPM by detecting the variations of axial forces at each actuation point instead of measuring their transverse deformations, which is difficult to achieve experimentally. The results demonstrated the decoupled CPM's excellent performances and also verified the effectiveness of the design method.

2. Structure Design of the 2-DOF CPM

The structure design, compared with geometric parameter optimization, will be more crucial and effective in guaranteeing the CPM's performance. As stated above, the input and output decoupling performances of the 2-DOF CPM are important and must be well guaranteed. Therefore, the structure of the CPM is determined according to the requirement of the decoupling characteristics in this section. The other performance indicators are ensured by resorting to the geometric parameter optimization in the following material. The schematic of the kinematic structure of the 2-DOF is depicted in Figure 1.
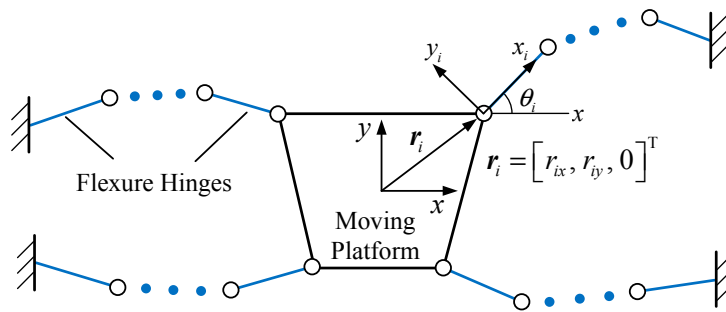
Figure 1. Kinematic structure of a 2-DOF CPM.

2.1. Realization of Output Decopuling Performance

The requirement of the output decoupling performance on the structure design of the 2-DOF CPM is studied first. It is expected that translational motion of the terminal platform along the *x*- and *y*-axes are independent, thereby ensuring the CPM with a total output decoupling characteristic. Therefore, the output stiffness matrix of the CPM should satisfy the form as

$$
\boldsymbol{K} = \begin{bmatrix} K_{x-Fx} & 0 & 0 \\ 0 & K_{y-Fy} & 0 \\ 0 & 0 & K_{\alpha-Mz} \end{bmatrix}
\tag{1}
$$

The output stiffness of the CPM can be calculated through the summation of the stiffness of each limb as [31]

$$
\boldsymbol{K} = \sum_{i=1}^{n} \boldsymbol{T}_{if}^{-1} \boldsymbol{K}_{i}^{l} \, \boldsymbol{T}_{id}^{-1}
\tag{2}
$$

where $\boldsymbol{K}_{i}^{l}$ is the local stiffness matrix of the *i*th limb, and $\boldsymbol{T}_{if}$ and $\boldsymbol{T}_{id}$ are the force and displacement transformation matrices, respectively, which take on the form

$$
\boldsymbol{T}_{if} = \boldsymbol{T}_{id}^{\mathrm{T}} = \begin{bmatrix} \cos\theta_i & -\sin\theta_i & 0 \\ \sin\theta_i & \cos\theta_i & 0 \\ r_{iy} & -r_{ix} & 1 \end{bmatrix}
\tag{3}
$$

The output stiffness matrix of the CPM should satisfy the form expressed in Equation (1). However, it is difficult to obtain a satisfied structure by solving the equations directly. To simplify this problem, the structure of the CPM is divided into two parts and the local coordinate systems of each subsystem are established, as shown in Figure 2. There are two ways to build the local coordinate systems, i.e., mirror symmetry and rotation symmetry.

The stiffness matrices of the two subsystems shown in Figure 2a under their corresponding local coordinate systems are expressed as

$$
\boldsymbol{K}_{i}^{\mathrm{m}} = \begin{bmatrix} K_{i-Fx}^{\mathrm{m}} & K_{ix-Fy}^{\mathrm{m}} & K_{ix-Mz}^{\mathrm{m}} \\ K_{iy-Fx}^{\mathrm{m}} & K_{1y-Fy}^{\mathrm{m}} & K_{iy-Mz}^{\mathrm{m}} \\ K_{i\alpha-Fx}^{\mathrm{m}} & K_{1\alpha-Fy}^{\mathrm{m}} & K_{i\alpha-Mz}^{\mathrm{m}} \end{bmatrix} \quad (i = 1,\,2)
\tag{4}
$$

Then, the stiffness matrix of the CPM under the globe coordinate system can be obtained according to Equation (2) as

$$
\boldsymbol{K}^{\mathrm{m}} = \sum_{i=1}^{2} \left(\boldsymbol{T}_{if}^{\mathrm{m}}\right)^{-1} \boldsymbol{K}_{i}^{\mathrm{m}} \left(\boldsymbol{T}_{id}^{\mathrm{m}}\right)^{-1}
\tag{5}
$$

where $\boldsymbol{T}_{1f}^{\mathrm{m}} = \left(\boldsymbol{T}_{1d}^{\mathrm{m}}\right)^{\mathrm{T}} = \mathrm{diag}([1,\,1,\,1])$, and $\boldsymbol{T}_{2f}^{\mathrm{m}} = \left(\boldsymbol{T}_{2d}^{\mathrm{m}}\right)^{\mathrm{T}} = \mathrm{diag}([-1,\,-1,\,1])$.
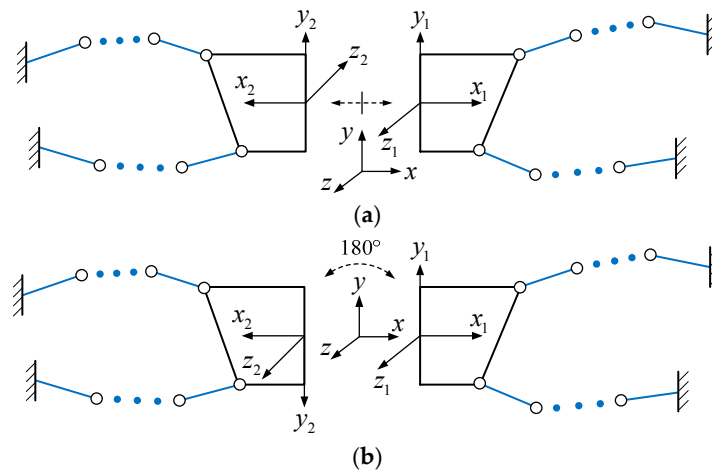
Figure 2. Division of a 2-DOF CPM: (**a**) mirror symmetry coordinate systems; and (**b**) rotation symmetry coordinate systems.

If the structure of the CPM is mirror symmetry, the local stiffness matrix of the two subsystems satisfies $\boldsymbol{K}_1^m = \boldsymbol{K}_2^m$. Then Equation (5) can be simplified as

$$\boldsymbol{K}^m = \begin{bmatrix} 2K_{1x-Fx}^m & 0 & 2K_{1x-Mz}^m \\ 0 & 2K_{1y-Fy}^m & 0 \\ 2K_{1\alpha-Fx}^m & 0 & 2K_{1\alpha-Mz}^m \end{bmatrix} \tag{6}$$

This shows that the translational motion along the y-axis will not affect the other two axes, while the translational motion along the x-axis and the rotational motion about the z-axis are coupled.

Similarly, when the structure of the CPM is rotation symmetry, its stiffness matrix can be obtained as

$$\boldsymbol{K}^s = \begin{bmatrix} 2K_{1x-Fx}^s & 2K_{1x-Fy}^s & 0 \\ 2K_{1y-Fx}^s & 2K_{1y-Fy}^s & 0 \\ 0 & 0 & K_{1\alpha-Mz}^s \end{bmatrix} \tag{7}$$

This indicates that the rotational motion about the z-axis has no influence on the other two axes, while the translational motions along the x- and y-axes are coupled.

It is verifiable that, when the structure of the CPM both satisfies the mirror and rotation symmetry, the translational and rotational motions of the terminal platform are independent. It is clear that the CPM is symmetric around the x- and y-axes when it satisfies both the mirror and the rotation symmetry. In order to obtain a total output decoupling characteristic, the actuation forces must be applied along the two symmetric axes at the same time. Therefore, linear actuators are needed, such as the piezoelectric actuator [32] and voice coil motor [33], which should be mounted along the symmetric axes. The above discussion shows that a symmetric kinematic structure can sufficiently ensure the 2-DOF CPM with total output decoupling performance.

2.2. Realization of Input Decopuling Performance

Next, the requirement of the input decoupling performance on the structure design of the 2-DOF CPM is investigated. The effective way of reducing the input coupling of the CPM is to adopt a flexure-based decoupler between an actuator and the terminal platform. There are two types of the decouplers, and their kinematic structures are shown in Figure 3.
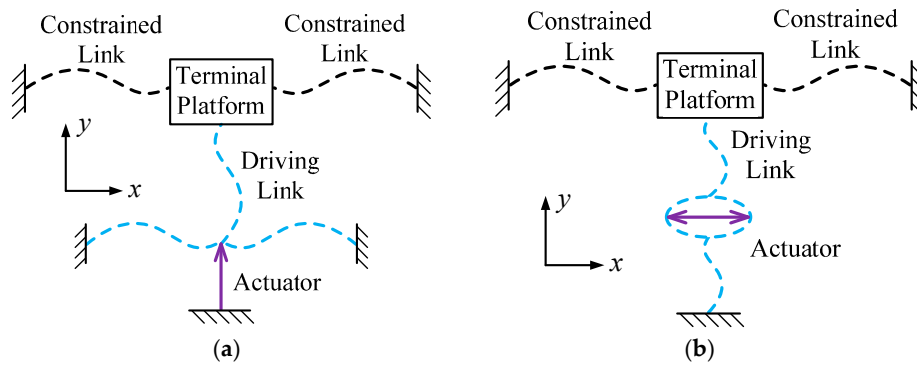
Figure 3. Kinematic structures of flexure-based decoupler. (**a**) Kinematic Structure 1. (**b**) Kinematic Structure 2.

The difference between the two decouplers is the actuator's mounting type. The actuator is fixed on the ground in the first decoupler, while the other installs the actuator on the moving part. The actuator can be inserted into a displacement amplifier in the second decoupler, which increases the motion stroke of the CPM and gives the actuator double protection from input coupling. However, this type of decoupler results in a more complex structure. Moreover, the actuator increases the moving mass of the CPM and thus reduces its natural frequency. Therefore, the first type of decoupler is preferred for this paper, and its detailed structure design will be investigated to guarantee the input decoupling characteristic of the CPM. Because of the symmetric structure of the 2-DOF CPM, we can choose the decoupler along the y-axis as the study object and its stiffness model is shown in Figure 4.
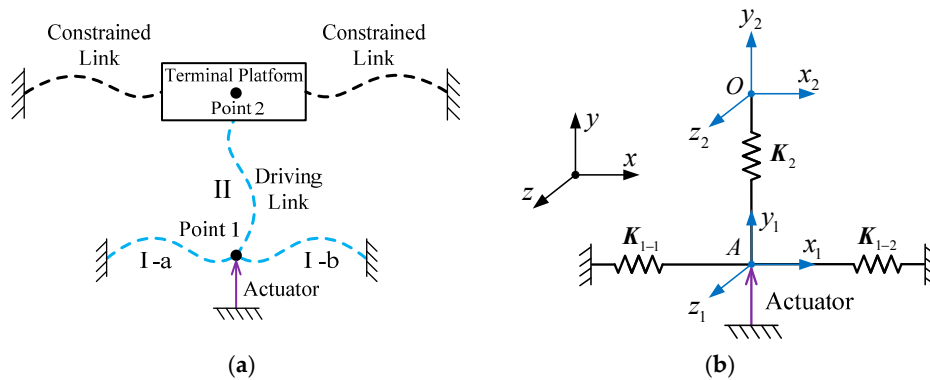
Figure 4. Stiffness model of flexure-based decoupler. (**a**) Kinematic structure. (**b**) Stiffness model.

For the 2-DOF CPM, excellent input decoupling performance requires that the transverse and rotational deformations at one actuation point are small enough that the terminal platform is actuated by the other actuator. According to Figure 4, utilizing a force equilibrium condition of point A_1 allows us to obtain the relationship between the displacement of the terminal platform and the deformation at the actuation point as

$$K_1 \delta_a + K_2(\delta_a - \delta_o) = 0 \quad \Rightarrow \quad \delta_a = (K_1 + K_2)^{-1} K_2 \delta_o \tag{8}$$

where δ_o is the is the displacement of the terminal platform, δ_a is the deformation of actuation point A_1, and K_1 and K_2 are the stiffness matrices of Parts I and II of the decoupler expressed in the coordinate frame $\{A\text{-}x_1 y_1 z_1\}$, respectively.

The bending and rotational deformations at the actuation point caused by the motion of the terminal platform can be obtained through the components of δ_a; they are expected to be as small as possible. Through a qualitative analysis of Equation (8), the stiffness requirement of the decoupler is:

the bending stiffness along the *x*-axis and the rotation stiffness about the *z*-axis of Part II should be much smaller than in Part I. With the exception of protecting the actuator from suffering transverse load, the decoupler also transmits the motion of the actuator to the terminal platform. Therefore, the axial stiffness along the *y*-axis of Part I should not be too large, in order to avoid the motion stroke of the actuator losing too much because of its deformation. In addition, the axial stiffness of Part II should be large in order to reduce the motion lost between the actuator and the terminal platform, thereby improving the motion transmission efficiency.

The design requirements on the decoupler will be utilized to guide its detailed structure design. The kinematic structure of Part I of the decoupler adopts a parallel type, as shown in Figure 5. In order to obtain a compact structure, the limb is constructed from a single leaf spring due to its advantages of compact size, lightweight, and easy manufacturing [34,35].
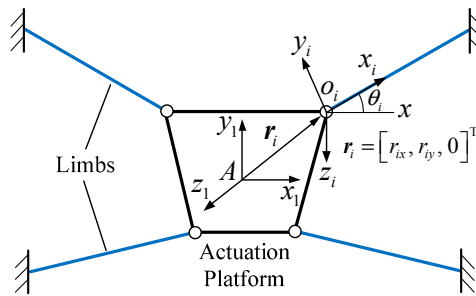
Figure 5. Kinematic structure of Part I of flexure-based decoupler.

The stiffness of Part I is the summation of the stiffness of each limb. Therefore, the influence of each limb's mechanical parameters on the stiffness of Part I is investigated first. The stiffness of the *i*th limb can be expressed in the coordinate system $\{A\text{-}x_1y_1z_1\}$ as

$$k_i^o = T_{if}^{-1} k_i^l T_{id}^{-1} \tag{9}$$

where k_i^l is the stiffness matrix of the *i*th limb expressed in its local coordinate frame $\{o\text{-}x_iy_iz_i\}$, which takes the form

$$k_i^l = \begin{bmatrix} k_{ix-Fx} & 0 & 0 \\ 0 & k_{iy-Fy} & k_{iy-Mz} \\ 0 & k_{i\alpha-Fy} & k_{i\alpha-Mz} \end{bmatrix} \tag{10}$$

The axial and bending stiffness of the limb can be obtained from Equation (9) as

$$k_{ix-Fx}^o = k_{ix-Fx} - \sin^2\theta_i \cdot \left(k_{ix-Fx} - k_{iy-Fy}\right) \tag{11}$$

$$k_{iy-Fy}^o = k_{ix-Fy} + \sin^2\theta_i \cdot \left(k_{ix-Fx} - k_{iy-Fy}\right) \tag{12}$$

Considering the stiffness components of the leaf spring satisfy $k_{ix-Fx} \gg k_{iy-Fy}$, the value of angle θ_i should be zero to ensure the large bending stiffness and small axial stiffness of Part I.

Then the rotation stiffness of the limb can be written as

$$k_{i\alpha-Mz}^o = r_{iy}^2 \cdot k_{ix-Fx} + r_{ix}^2 \cdot k_{iy-Fy} + k_{i\alpha-Mz} + 2r_{ix} \cdot k_{iy-Mz} \tag{13}$$

Because each component of the stiffness matrix k_i^l is greater than zero, the increment of r_{ix} and r_{iy} will both increase the rotation stiffness.

According to the discussion above, in order to meet the stiffness requirement of Part I of the decoupler, each limb should be parallel to the *x*-axis and their positions should be far from the centric of the actuation platform if possible.

Next, the influence of the leaf spring's geometric parameters is studied. The stiffness matrix of a single leaf spring can be expressed as

$$
\boldsymbol{k}_L = \begin{bmatrix} \frac{EDt}{L} & 0 & 0 \\ 0 & \frac{EDt^3}{L^3} & \frac{EDt^3}{2L^2} \\ 0 & \frac{EDt^3}{2L^2} & \frac{EDt^3}{3L} \end{bmatrix} \tag{14}
$$

where E is the elastic modulus, and L, t, and D are the length, thick and height of the leaf spring, respectively.

According to the stiffness requirement of Part I and the above analysis, the bending stiffness of the leaf spring should be small, while the axial and rotation stiffness should be large. According to Equation (13), however, it is impossible to reduce the bending stiffness of the single leaf spring while guaranteeing that the axial and rotation stiffness remain unchanged or increased by adjusting its geometric parameters. Therefore, another type of hinge should be proposed to construct a satisfied limb. As opposed to utilizing a single flexure hinge, a compound hinge composed of n identical parallel leaf springs is chosen, as shown in Figure 6.

(**a**)   (**b**)
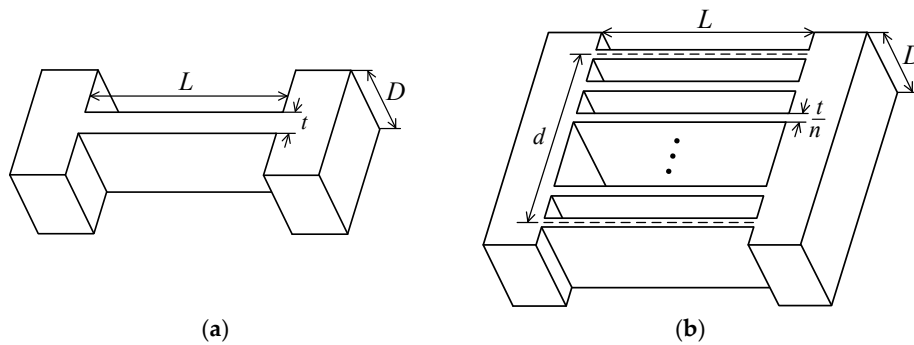
Figure 6. Single and compound leaf springs. (**a**) Single leaf spring. (**b**) Compound leaf spring.

The length, height and total mass of the compound hinge are the same as the single leaf spring, and its stiffness matrix can be expressed as

$$
\boldsymbol{K}_n = \begin{bmatrix} k_{1x-Fx} & 0 & 0 \\ 0 & (1/n)^2 \cdot k_{1y-Fy} & (1/n)^2 \cdot k_{1y-Mz} \\ 0 & (1/n)^2 \cdot k_{1\alpha-Fy} & \left((n+1)/(n-1) \cdot \gamma^2 + (1/n)^2 \right) \cdot k_{1\alpha-Mz} \end{bmatrix} \tag{15}
$$

where $\gamma = d/2t$, and k_{1m-n} is the stiffness component of the single leaf spring.

Equation (14) shows that the axial stiffness of the compound hinge is equal to the single leaf spring, and the bending stiffness is always smaller and decreases rapidly as number n grows. The rotation stiffness depends on the number n and parameter γ. When $\gamma > 1$, the rotation stiffness is always larger than that of a single leaf spring. Therefore, the compound hinge will meet that requirement quite well.

Because the stiffness requirement of Part II of the decoupler is contrary to Part I, its limbs should be parallel to the y-axis according to the investigation above. The leaf spring is still utilized to construct the limbs in Part II and its stiffness requirement is illustrated as: the axial stiffness should be large while the bending and rotation stiffness should be small. The heights of the flexure hinges adopted in Parts I and II are the same due to the monolithic structure of the CPM. In this case, no matter what, the single leaf spring and the compound hinge cannot meet the stiffness requirement. Considering the terminal platform of the 2-DOF CPM only has the translation motion, minimizing the bending stiffness and shear stiffness k_{a-Fy} can ensure the decoupler with an excellent decoupling character according to Equation (8). The bending and shear stiffness of the compound hinge all decrease sharply

as the number *n* grows. Therefore, the compound hinge is still the best choice when constructing the limbs of Part II of the decoupler.

As mentioned above, the excellent input decoupling character requires that the bending and shear stiffness of the compound hinges of Part II are small, and the axial and rotation stiffness of the compound hinge of Part I are large. Except for the axial stiffness, the other stiffness components of the compound hinge will all decrease as number *n* increases. Therefore, the number *n* of the compound hinge of Part I would be greater than that of Part II. In addition, the number *n* of the compound hinge should not be overly large, due to difficulties in manufacturing and because it is then prone to buckling under axial load. Taking all these factors into consideration, the number *n* of the compound hinges of Parts I and II are chosen to be two and three respectively in this paper.

2.3. Detailed Structure of the 2-DOF CPM

According to the discussion above, the detailed structure of the 2-DOF CPM is given in Figure 7. The output decoupling performance of the CPM is realized by the symmetric kinematic structure, and the input coupling is reduced by the flexure-based decoupler composed of the compound hinges.
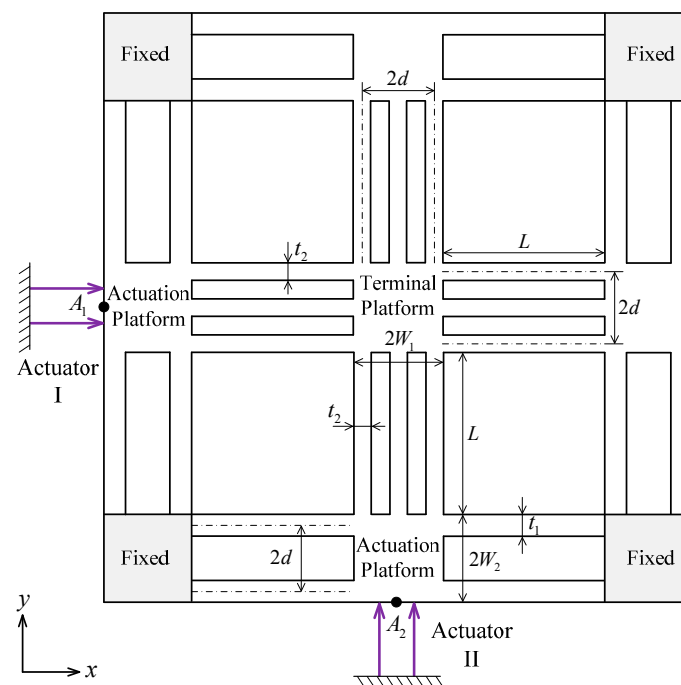
Figure 7. Detailed structure of 2-DOF CPM.

3. Analytical Modeling of the 2-DOF CPM

The detailed structure of the 2-DOF CPM has already been determined to guarantee the decoupling performances, and in this section its geometric parameters will be optimized to obtain an ideal mechanism. With the exception of decoupling performance, the concerned performance indicators also include the input and output stiffness, motion stroke, and natural frequency. Their analytical models should be established before optimization.

3.1. Input and Output Stiffness

The stiffness model of the 2-DOF CPM is given in Figure 8a, and the input and output stiffness matrices will be derived first. Because the stiffness modeling is related to specific coordinate frames, the globe coordinate frame is defined at the center of the terminal platform and the local coordinate systems of each chain are shown in Figure 8b.
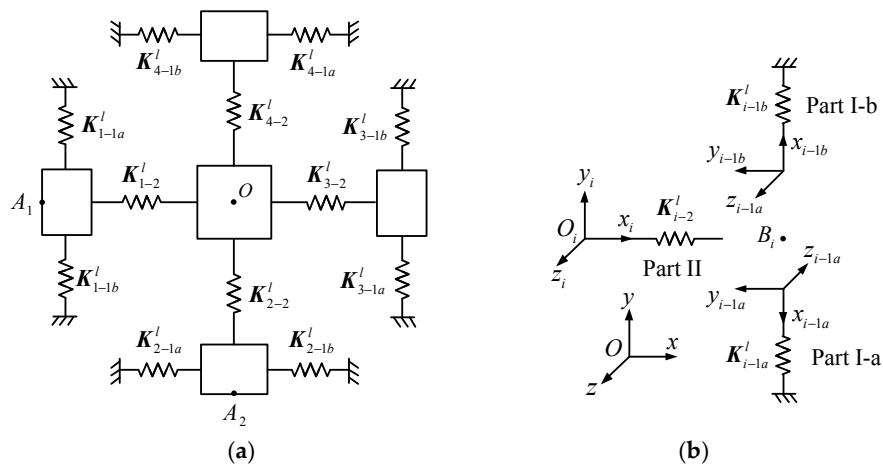
Figure 8. Stiffness model and coordinate frames of 2-DOF CPM. (**a**) Stiffness model of the CPM. (**b**) Stiffness model of a chain.

The matrix method [36,37], which has the advantages of terse form and high modeling accuracy, has already been widely utilized in the stiffness modeling of the compliant mechanism. Therefore, it is adopted to establish the analytical model of the 2-DOF CPM. To unify the description of the stiffness matrices in this paper, we utilize $K_{i-m}{}^l$ and $^P K_{i-m}$ to represent the stiffness of Part m in the ith chain expressed in its local coordinate frame and the coordinate frame $\{P\}$. The stiffness expressed in different coordinate frames can be transformed through the following expression as

$$^Q K = T_f^{-1}{}^P K\, T_d^{-1} \tag{16}$$

where T_f and T_d are the force and displacement transformation matrices between the coordinate frames $\{P\}$ and $\{Q\}$.

The stiffness matrices of Parts I and II of each chain under their local coordinate frames are calculated first. These two parts consist of compound hinges; the geometric parameters of the hinges and their local coordinate frames are shown in Figure 9.
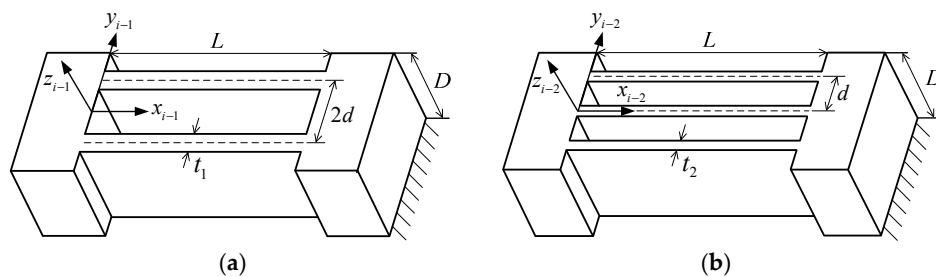
Figure 9. Geometric parameters and local coordinate frames of Parts I and II. (**a**) Part I. (**b**) Part II.

According to Equation (14), the stiffness of the two parts can be obtained, respectively, as

$$K_{i-1a}^l = K_{i-1b}^l = \begin{bmatrix} \frac{2EDt_1}{L} & 0 & 0 \\ 0 & \frac{2EDt_1^3}{L^3} & \frac{EDt_1^3}{L^2} \\ 0 & \frac{EDt_1^3}{L^2} & \left(6\left(\frac{d}{t_1}\right)^2 + 2\right) \cdot \frac{EDt_1^3}{3L} \end{bmatrix} \tag{17}$$

$$K_{i-2}^l = \begin{bmatrix} \frac{3EDt_2}{L} & 0 & 0 \\ 0 & \frac{3EDt_2^3}{L^3} & \frac{3EDt_2^3}{2L^2} \\ 0 & \frac{3EDt_2^3}{2L^2} & \left(6\left(\frac{d}{t_2}\right)^2 + 3\right) \cdot \frac{EDt_2^3}{3L} \end{bmatrix} \tag{18}$$

The chain of the CPM is composed of Parts I and II connected in series; therefore, its compliance matrix under its local coordinate frames $\{O_i\}$ can be calculated as

$$^{O_i}C_i = \left(^{O_i}K_{i-1a} + {}^{O_i}K_{i-1b}\right)^{-1} + {}^{O_i}K_{i-2}^{-1} \tag{19}$$

The CPM is composed of the four identical chains connected in parallel type, and its output stiffness can be obtained as

$$K_{\text{output}} = \sum_{i=1}^{4} {}^{O}T_i^{-1} \left(^{O_i}K_i\right) {}^{O}T_i^{-T} \tag{20}$$

where ${}^{O}T_1 = \begin{bmatrix} -1 & 0 & 0 \\ 0 & -1 & 0 \\ 0 & W_1 & 1 \end{bmatrix}$, ${}^{O}T_2 = \begin{bmatrix} 0 & 1 & 0 \\ -1 & 0 & 0 \\ -W_1 & 0 & 1 \end{bmatrix}$, ${}^{O}T_3 = \begin{bmatrix} 1 & 0 & 0 \\ 0 & 1 & 0 \\ 0 & -W_1 & 1 \end{bmatrix}$, and

${}^{O}T_4 = \begin{bmatrix} 0 & -1 & 0 \\ 1 & 0 & 0 \\ W_1 & 0 & 1 \end{bmatrix}$.

The input stiffness of the 2-DOF CPM along its two axes is identical. The input stiffness model of the CPM in the *x*-axis is depicted in Figure 10, where ${}^{O}K_{T1}$ is the total stiffness of three chains from the second to the fourth chain and can be obtained as

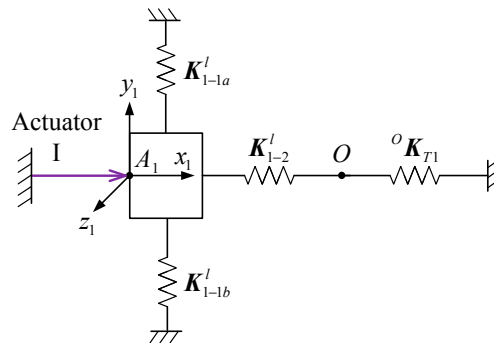$$^{O}K_{T1} = \sum_{i=2}^{4} {}^{O}T_i^{-1} \left(^{O_i}K_i\right) {}^{O}T_i^{-T} \tag{21}$$

Figure 10. Input stiffness model of CPM in the *x*-axis.

The input stiffness of the CPM can be obtained according to Figure 11 as

$$K_{\text{Input}} = {}^{A_1}K_{1-1a} + {}^{A_1}K_{1-1b} + \left({}^{A_1}K_{1-2}^{-1} + {}^{A_1}T^{T}\left(^{O}K_{T1}^{-1}\right){}^{A_1}T\right)^{-1} \tag{22}$$

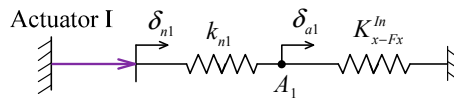where ${}^{A_1}T = \begin{bmatrix} 1 & 0 & 0 \\ 0 & 1 & 0 \\ 0 & L + W_1 + 2W_2 & 1 \end{bmatrix}$.

Figure 11. Input stiffness model of CPM considering the stiffness of the actuator.

3.2. Motion Stroke

The motion strokes along the *x*- and *y*-axes of the 2-DOF CPM are the same. Considering the stiffness of the actuator, the input stiffness of the CPM in the *x*-axis is given in Figure 11.

The relationship between the actual and nominal displacement output of the actuator can be obtained according to Figure 11 as

$$\delta_{a1} = \frac{k_{n1}}{k_{n1} + K_{x-Fx}^{In}} \cdot \delta_{n1} = \frac{1}{1 + K_{x-Fx}^{In}/k_n} \cdot \delta_{n1} \tag{23}$$

where k_{n1} is the axial stiffness of the actuator, and K_{x-Fx}^{In} is the input axial stiffness of the CPM along the *x*-axis.

The efficiency of the motion transferred from the actuation point to the terminal platform should also be calculated to obtain the motion stroke of the CPM. According to Figure 10, utilizing a force equilibrium condition of point *O* can obtain the relationship between the displacement output of the terminal platform and the deformation at the actuation point A_1 as

$$^{O}K_{T1}\delta_o + {}^{O}K_{1-2}(\delta_o - \delta_{a1}) = 0 \quad \Rightarrow \quad \delta_o = \left[\left({}^{O}K_{1-2} + {}^{O}K_{T1} \right)^{-1} {}^{O}K_{1-2} \right] \delta_{a1} \tag{24}$$

The motion stroke of the CPM along the *x*-axis can be calculated according to Equations (22) and (23) as

$$\delta_{ox} = \frac{\left[\left({}^{O}K_{1-2} + {}^{O}K_{T1} \right)^{-1} {}^{O}K_{1-2}e_1 \right]^{\mathrm{T}} e_1}{1 + K_{x-Fx}^{In}/k_n} \cdot \delta_n \tag{25}$$

where $e_1 = [1, 0, 0]^{\mathrm{T}}$ is a unit vector.

Additionally, the maximum stress generated inside the flexure hinges should be kept within the allowable value when the CPM moves to the maximum displacement. The maximum stress of Parts I and II can be calculated as [22]

$$\sigma_1^{\max} = \alpha \frac{12\delta_a^{\max} E t_1}{L^2} \leq \frac{\sigma_y}{n} \, , \, \sigma_2^{\max} = \alpha \frac{12\delta_o^{\max} E t_2}{L^2} \leq \frac{\sigma_y}{n} \tag{26}$$

where α is the stress concentration factor chosen as 2, $\delta_a^{\max}$ and $\delta_o^{\max}$ are the maximum displacements of the actuation platform and terminal platform, σ_y is the yield stress of the material, and *n* is the safety factor chosen as 1.5.

According to Equation (23), the maximum displacement of the terminal platform is always smaller than that of the actuation platform. Therefore, the motion stroke of the CPM should satisfy

$$\delta_o^{\max} \leq \min\left\{ \frac{\sigma_y L^2}{12n\alpha E t_1} \, , \, \frac{\sigma_y L^2}{12n\alpha E t_2} \right\} \tag{27}$$

3.3. Decoupling Character

The symmetric structure of the 2-DOF CPM has already ensured it with a total output decoupling performance. Therefore, only the analytical model for the input decoupling characteristic is investigated and evaluated using the ICD. Without loss of generality, the ICD of the 2-DOF CPM can

be defined using the ratio of the bending deformation at the actuation point A_2 along the x-axis to the axial deformation at the actuation point A_1 along the x-axis when only Actuator I is actuated.

The relationship between the displacement output of the terminal platform and the deformation at the actuation point A_1 has already been obtained in Equation (23). Then the deformation at the actuation point A_2 caused by the motion of the terminal platform must be calculated to obtain the ICD of the CPM. The stiffness model of the CPM along the y-axis is given in Figure 12, where ${}^{O}K_{T2}$ is the total stiffness of the first, third and fourth chains.
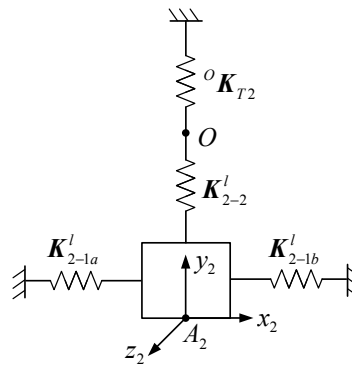
Figure 12. Stiffness model of CPM along the y-axis.

Similarly, the relationship between the deformation at the actuation point A_2 and the displacement of the terminal platform can be obtained by resorting to a force equilibrium condition of point A_2 as

$$\delta_{a2} = \left[\left({}^{A_2}K_{2-1a} + {}^{A_2}K_{2-1b} + {}^{A_2}K_{2-2}\right)^{-1}{}^{A_2}K_{2-2}\right]\delta_o \tag{28}$$

Combining Equations (23) and (27), the relationship between the deformations at two actuation points when only Actuator I is driven can be obtained as

$$\delta_{a2} = \left({}^{A_2}K_{2-1a} + {}^{A_2}K_{2-1b} + {}^{A_2}K_{2-2}\right)^{-1}{}^{A_2}K_{2-2}\left({}^{O}K_{1-2} + {}^{O}K_{T1}\right)^{-1}{}^{O}K_{1-2}\delta_{a1} \tag{29}$$

Therefore, the analytical model of the ICD of the 2-DOF CPM can be defined as

$$ICD = \left[\left({}^{A_2}K_{2-1a} + {}^{A_2}K_{2-1b} + {}^{A_2}K_{2-2}\right)^{-1}{}^{A_2}K_{2-2}\left({}^{O}K_{1-2} + {}^{O}K_{T1}\right)^{-1}{}^{O}K_{1-2}e_1\right]^{\mathrm{T}}e_1 \tag{30}$$

3.4. Natural Frequency

In order to ensure the excellent dynamic property of the CPM, its mechanical natural frequency should be large. The first two natural frequencies of the 2-DOF CPM are identical, and the corresponding vibration motions should be the translational modes along the two axes. Owing to the adopted decoupler, the coupling effects between the actuators of the CPM can be ignored. Therefore, the translational mode along the x-axis can be depicted as shown in Figure 13, where m_a and m_o are the masses of the actuation platform and terminal platform, respectively, and m_1 and m_2 are the masses of the single leaf spring in Parts I and II, respectively.
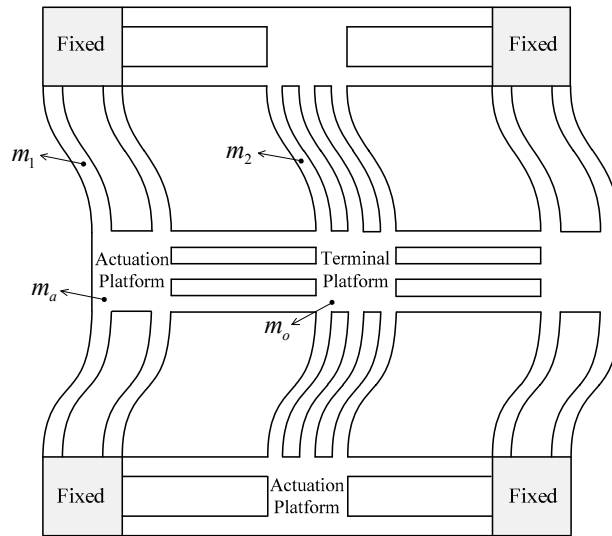
Figure 13. Translational mode along the *x*-axis of 2-DOF CPM.

Due to the continuum structure of the CPM, its dynamic response analysis should utilize the partial differential equation models which are difficult to solve. Considering that the axial stiffness of Part II of each chain is large, the displacements of the actuation platform, terminal platform and Part II of the first and third chains can be considered to be almost identical in the translational mode along the *x*-axis. Therefore, the CPM is equivalent to a generalized single degree-of-freedom (SDOF) system in this vibration mode, as shown in Figure 14.
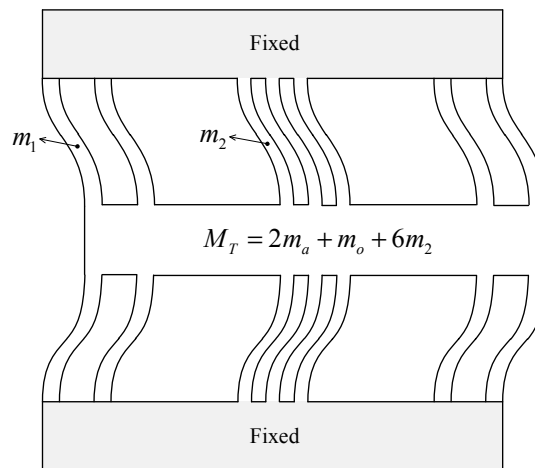
Figure 14. Translational mode of an equivalent generalized SDOF system.

The Rayleigh method can be utilized to calculate the natural frequency of the equivalent SDOF system as

$$f = \frac{1}{2\pi}\sqrt{\frac{K_{\text{eq}}}{M_{\text{eq}}}} \tag{31}$$

where K_{eq} and M_{eq} are the equivalent stiffness and mass of the system.

The equivalent stiffness of the SDOF can be obtained as

$$K_{\text{eq}} = 8\int_0^L EI_1(x)[\psi''(x)]^2 dx + 6\int_0^L EI_2(x)[\psi''(x)]^2 dx \tag{32}$$

where $I_1(x)$ and $I_2(x)$ are the moment of inertia of the single leaf spring in Parts I and II, respectively, and $\psi(x)$ is the shape function.

The equivalent mass of the SDOF system can be obtained as

$$M_{\text{eq}} = M_T + M_f \tag{33}$$

where $M_T = 2m_a + m_o + 6m_2$ is the mass of the rigid moving part, and M_f is the equivalent mass of the flexure members, which

$$M_f = 8\int_0^L m_1(x)[\psi(x)]^2 dx + 6\int_0^L m_2(x)[\psi(x)]^2 dx \tag{34}$$

The calculation accuracy of the natural frequency of the SDOF system depends on the authenticity of the estimated shape function. According to the constraint characteristics, the flexure members in the translational vibration mode can be treated as fixed-fixed beams. Therefore, the shape function can be determined as shown in Figure 15, where the rotational angles of both ends under the applied loads equal to zero.
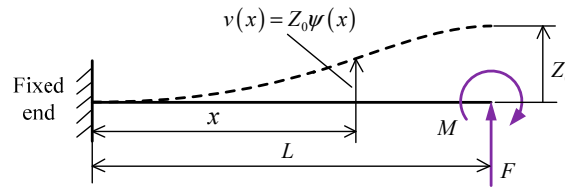
Figure 15. Determination of the shape function.

According to Figure 15, the shape function of the flexure members can be determined as

$$\psi(x) = \frac{v(x)}{Z_0} = \frac{3x^2}{L^2} - \frac{2x^3}{L^3} \tag{35}$$

Substituting Equation (34) in Equations (31) and (32) can obtain the equivalent stiffness and mass of the SDOF system as

$$K_{\text{eq}} = \frac{8EDt_1^3}{L^3} + \frac{6EDt_2^3}{L^3} \tag{36}$$

$$M_{\text{eq}} = 2m_a + m_o + \frac{104}{35}m_1 + \frac{288}{35}m_2 \tag{37}$$

4. Geometric Parameters Optimization and Performance Evaluation

4.1. Geometric Parameters Optimization

To ensure the excellent performances of the 2-DOF CPM, it is necessary to optimize its geometric parameters. The optimum goal is to guarantee the excellent decoupling performance of the CPM. Because the symmetric structure of the CPM already possesses a total output decoupling character, the minimization of the input coupling will be selected as the optimization objective, i.e., min (*ICD*). The CPM is fabricated from a single block with a specific thickness of 15 mm, and the independent geometric parameters to be optimized are L, t_1, t_2, and d. The other performances of the CPM, including the workspace, output rotation stiffness, and natural frequency, are guaranteed by the constraint conditions described as follows.

(1)　Workspace: $\delta_x \times \delta_y \geq 47.5~\mu\text{m} \times 47.5~\mu\text{m}$. According to the analytical models, the workspace of the CPM is influenced by the stiffness of the actuator and the mechanism, and is also limited by the maximum stress of the materials. The nominal motion stroke of the piezoelectric actuator

adopted in this CPM is 60 μm, and its static axial stiffness is about 15 N/μm. Additionally, alloy Al-7075 with a yield stress of 525 MPa is chosen to fabricate the CPM. According to the given workspace, Equations (24) and (26) can be utilized to determine the satisfied ranges of the geometric parameters.

(2)   Output rotation stiffness: $K_\alpha \geq 3.5 \times 10^4$ Nm/rad. The translational deformations of the terminal platform caused by external loads along the *x*- and *y*-axes can be compensated through the closed-loop control. However, the rotational deformation about the *z*-axis cannot be compensated, and thus will affect the motion precision of the CPM. Therefore, the output rotation stiffness is expected to be large enough.

(3)   Natural frequency: $f \geq 800$ Hz. The first two natural frequencies of the 2-DOF CPM are identical and correspond to the translational vibration modes along the two axes. Therefore, they should be as high as possible to guarantee the CPM with a rapid dynamic response and robustness against the disturbances.

The optimization process of the CPM's geometric parameters is performed with the "fmincon" function. It is an optimization function in MATLAB used to find a constrained minimum of a scalar function of several variables and its grammar is given as

$$[x, \text{fval}] = \text{fmincon}(fun, x0, A, b, Aeq, beq, lb, ub, \text{nonlcon}) \tag{38}$$

where x is the optimized solution, fval is the value of the objective function at the solution x, fun is the objective function, $x0$ is the initial point for x, A is the matrix for linear inequality constraints, b is the vector for linear inequality constraints, Aeq is the matrix for linear equality constraints, beq is the vector for linear equality constraints, lb is the vector of lower bounds, ub is the vector of upper bounds, and nonlcon is the nonlinear constraint function.

The minimization of the ICD is adopted as the objective function and the requirement of the workspace, output rotation stiffness, and the natural frequency of the CPM are used as the nonlinear constraint conditions in the "fimincon" function. There are no linear inequality and linear equality constraints in the geometric parameters optimization, and therefore set $A = []$, $b = []$, $Aeq = []$, $beq = []$. Additionally, the ranges of the geometric parameters are given as 50 mm $\leq L \leq$ 75 mm, 1 mm $\leq t_1 \leq$ 5 mm, 1 mm $\leq t_2 \leq$ 5 mm, 5 mm $\leq d \leq$ 10 mm, and their initial values are given as $L = 60$ mm, $t_1 = 3$ mm, $t_2 = 3$ mm, and $d = 7.5$ mm. Finally, the optimized parameters are obtained as $L = 50$ mm, $t_1 = 3.56$ mm, $t_2 = 2.57$ mm, and $d = 10$ mm. The ICD of the optimized CPM is as low as 0.279%, which indicates that the 2-DOF CPM possesses an excellent input decoupling character. The analytical results of other performance indicators are also obtained. The results show that the CPM has a workspace of 47.54 μm $\times$ 47.54 μm. The input and output stiffness are 3.68 N/μm and 3.50×10^4 Nm/rad, respectively. In addition, the natural frequency is 876 Hz. The analytical results show that the key performances of the optimized CPM all satisfy the design requirements.

4.2. Performance Evaluation with Finite Element Analysis

The optimized mechanism's performance will be evaluated through FEA, performed with the ANSYS WorkBench software (Workbench 14.5, ANSYS Inc., Cannonburg, PA, USA). The physical and mechanical parameters of the adopted material alloy Al-7075 are: Young's modulus = 71.7 GPa, Poisson's ratio = 0.33, Density = 2770 kg/m^3, and yield stress = 525 MPa.

A good finite element model with a reasonably high number of DOFs is first required to guarantee the accuracy of FEA results. The finite element model of the CPM is presented in Figure 16, wherein the mesh is generated by using the hex dominant method. The maximum element size is set as 2 mm and the numbers of the nodes and elements are 139,471 and 32,016, respectively.
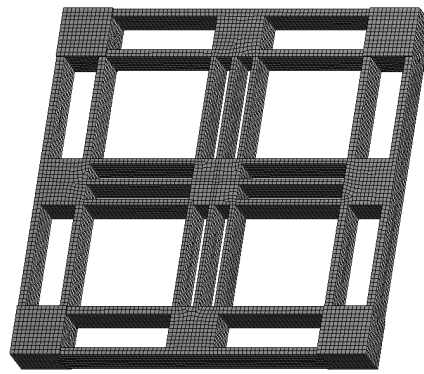
Figure 16. Finite element model of the CPM.

The input axial stiffness of the CPM is calculated by applying a force at the actuation point A_1, as shown in Figure 17a. The relationship between the applied force and the deformation at point A_1 is obtained and is given in Figure 17b. The force–displacement curve fits into a line very well, which indicates the linearity of the CPM. The input axial stiffness is obtained by calculating the slope of the fitted line and resorting to the least squares method, which is 3.36 N/μm. In actual CPM, preloading and actuation forces will cause initial displacements along each axis, which may influence the CPM's stiffness. Taking a small initial displacement (less than 100 μm) along one axis into consideration, both the theoretical and finite element models have demonstrated that the CPM's stiffness remains unchanged.

(**a**)　　　　　　　　　　　　　　　　　　　(**b**)
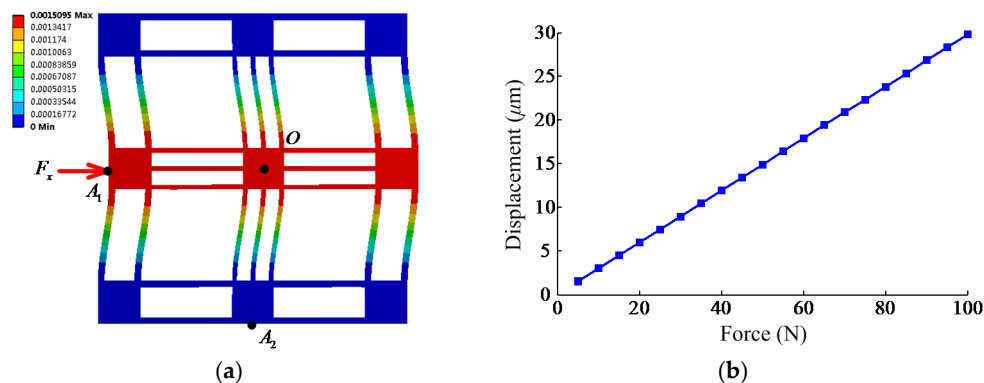
Figure 17. Finite element model and results of input axial stiffness. (**a**) Finite element model. (**b**) Force-displacement curve.

Similarly, the output rotation stiffness of the CPM can be analyzed through applying bending moment at the terminal platform, as shown in Figure 18a. The relationship between the rotation angle and applied moment is given in Figure 18b, and the output rotation stiffness can be calculated as 3.33×10^4 Nm/rad.

It can be observed that the input axial stiffness and the output rotation stiffness of the CPM calculated through FEA are 8.7% and 4.9% smaller than the theoretical values. The reason is because the actuation platform and terminal platform are considered to be rigid parts in the analytical model, but they also suffer deformation under the applied loads. This is evident from the stress distribution diagrams shown in Figure 19. Therefore, the compliance of the platforms reduces the stiffness of the CPM.
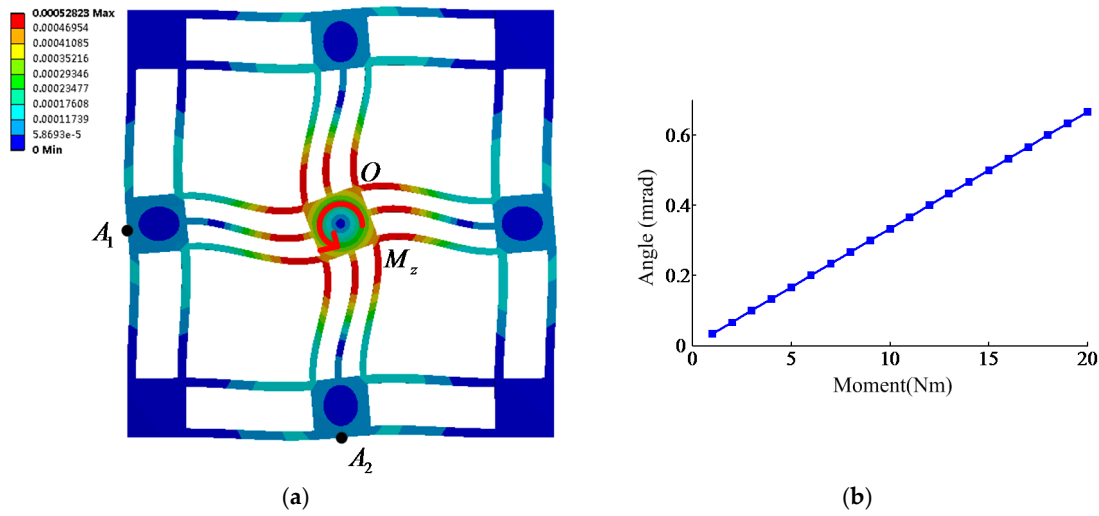
Figure 18. Finite element model and results of output rotation stiffness. (**a**) Finite element model. (**b**) Force-displacement curve.
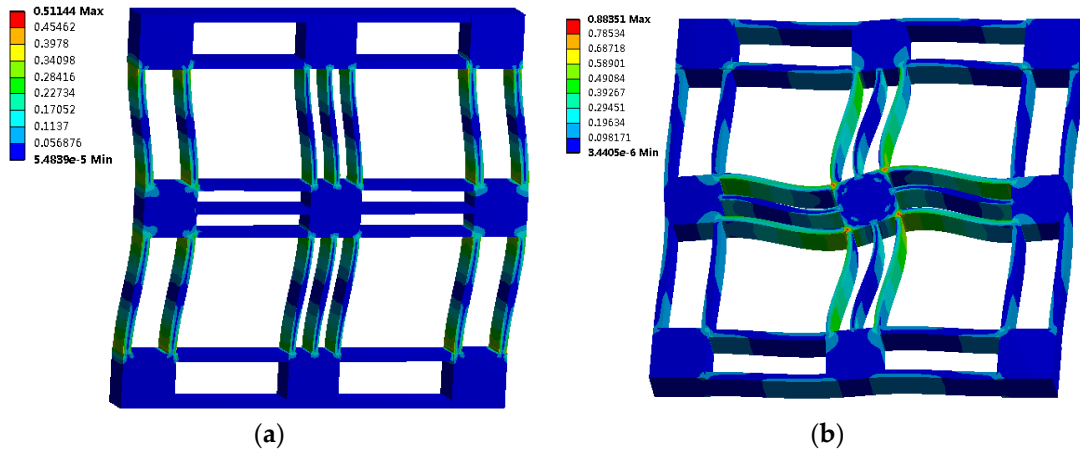

Figure 19. Stress diagrams of the CPM under applied force and moment. (**a**) Stress diagram related to the axial force. (**b**) Stress diagram related to the moment.

The finite element model shown in Figure 17a can be utilized to calculate the ICD of the CPM. When the driving force 100 N is applied at the actuation point A_1 along the x-axis, the axial deformation at point A_1 and the bending deformation at point A_2 are 29.8 μm and 8.66×10^{-2} μm, respectively. The ICD can be calculated as 0.291%, which is close to the theoretical value. This not only verifies the validity of the analytical model but also demonstrates the excellent input decoupling characteristic of the CPM.

Furthermore, the resonant frequencies and corresponding vibration modes of the CPM are also simulated. The first six natural frequencies are 808 Hz, 808 Hz, 1802 Hz, 3153 Hz, 3153 Hz, and 3430 Hz, and the first three vibration modes are shown in Figure 20. The simulation results show that the first two natural frequencies are identical, and their vibration modes exist along the x- and y-axes, which correspond to the structural characteristic of the CPM. The third vibration mode is out-of-plane motion and its frequency is more than twice as large as the first two natural frequencies. Additionally, the rotational vibration mode corresponds to the eighth vibration mode with a frequency of 4636 Hz. Therefore, the vibration modes with higher frequencies have less of an effect on the translation motion of the CPM. Compared with the simulation results, the analytical model overestimates the first two natural frequencies with a derivation of 8.4%. This may arise from an overestimation of the equivalent

stiffness in Equation (30). The more accurate equivalent stiffness can be replaced by the simulated input axial stiffness, and the first two natural frequencies can be calculated as 805 Hz, which is close to the simulation result.
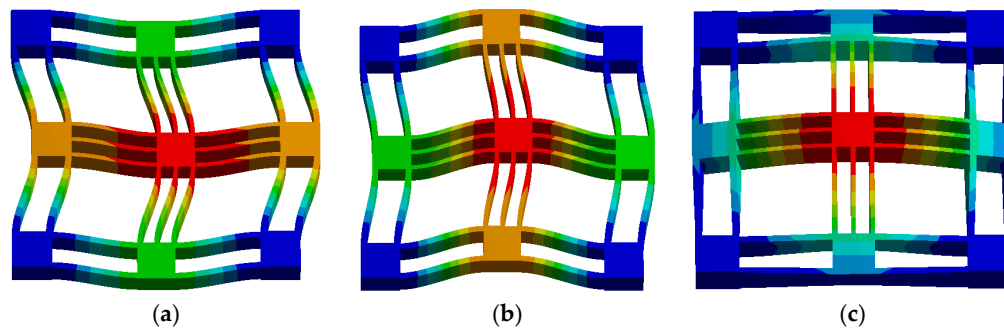

| (a) | (b) | (c) |

Figure 20. First three vibration modes of the CPM. (**a**) First mode. (**b**) Second mode. (**c**) Third mode.

5. Experimental Test

In this section, a prototype of the 2-DOF CPM was fabricated and several experimental tests were carried out to evaluate its performance and demonstrate the effectiveness of the proposed design method. Referring to the optimized results, the dimensions of the prototype were selected as: L = 50 mm, t_1 = 3.5 mm, t_2 = 2.5 mm, and d = 10 mm. The 3-D model and the experimental table of the 2-DOF CPM are shown in Figure 21. The main body of the CPM was fabricated using the milling process with a single block of Al-7075. From the stress diagrams shown in Figure 19, we can see there is a concentration of stress where the leaf springs connect to the platforms and the fixed base. Therefore, fillets with a 2 mm radius were machined at both ends of the flexure members to reduce the effects of stress concentration. Two 60-μm-stroke piezoelectric actuators (P-843.40 from Physik Instrument) were adopted to drive the stage. They were driven by a modular piezo controller & driver (E-621 from Physik Instrument), which generates voltage up to 120 V. Two force sensors (U93-1kN from HBM) were mounted at the end of each actuator to detect their actuation forces. Compared to mounting them in front of the actuators, this installation type reduces the moving mass of the stage and thus improves its dynamic response. A four-channel high dynamic signal processor (MX410 from HBM) was utilized to amplify and record the analog voltage output of the force sensors. The displacement outputs of the terminal platform along the two axes were measured using two high precision length gauges (MT-1281 from Heidenhain). A DSPACE processor board DS1007 equipped with a 16-bit ADC card (DS2004), a 16-bit DAC card (DS2101), and a six-channel incremental encoder interface card (DS3002) was utilized to output the excitation voltage for the piezo servo controller and capture the data from the force sensor signal processor and length gauges. Preloads were applied along the two axes through preload baffles to prevent the piezoelectric actuators from suffering pulling forces during the motion process and to eliminate the clearances between the actuators and the mechanism. The preloading forces were detectable by the force sensors and they were set to about 300 N initially.

The input axial stiffness along the two axes was tested first. The actuation forces were detected using the force sensors and the displacements were measured using the length gauges. Figure 22 shows the relationship between the tested actuation forces and the corresponding displacements along the two axes. The tested displacement–force curves fit into lines well and indicate the stiffness of the CPM is linear, which will be easy to control. The least squares method was utilized to fit the results and the input axial stiffness of the CPM was calculated as 3.87 N/μm and 3.93 N/μm, respectively. The axial stiffness measurements were greater than the theoretical and simulated results. The differences occur for two reasons. First, the fillets machined at both ends of the leaf springs increase their stiffness. Second, the displacement output of the terminal platform is larger than that measured at the actuation point, which results in a larger measured stiffness.
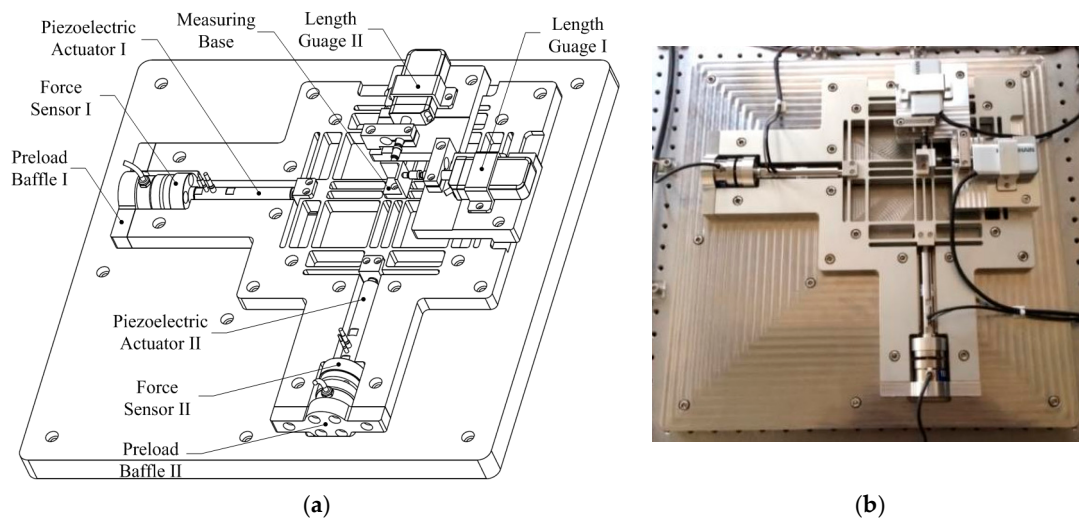
(**a**)　　　　　　　　　　　　　　　　　　　　　　　(**b**)

Figure 21. 3-D model and prototype of 2-DOF CPM. (**a**) 3-D model. (**b**) Prototype.
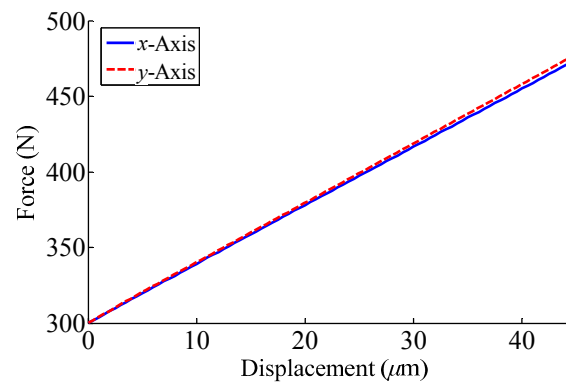

Figure 22. Experimental results of input axial stiffness.

The workspace of the CPM was tested through running a square trajectory in the open-loop control. The experimental result and estimated workspace are given in Figure 23. The measured workspace was 45.21 μm × 45.63 μm, which is a little smaller than the estimated result. The decreased motion of the CPM lies in the deformations of the joint surfaces between the parts connected by bolts.
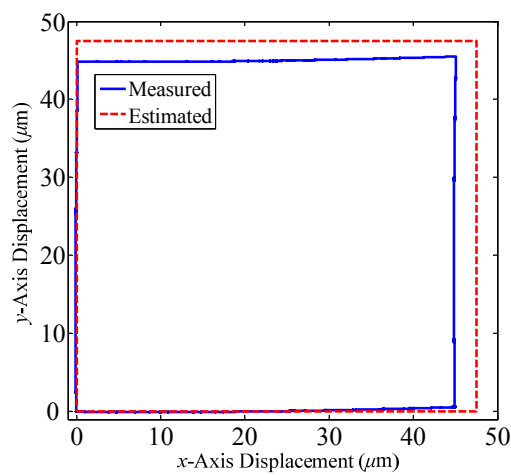
Figure 23. Workspace of 2-DOF CPM.

Then the natural frequency of the CPM was tested using the hammering method with the piezoelectric actuators dismantled. A modal hammer was utilized to apply impulse forces at the actuation points along the two axes, respectively. The dynamic response of the terminal platform was captured by the length gauges and the spectral analyses on the experimental results have been given in Figure 24. The first two natural frequencies of the CPM were obtained as 793 Hz and 799 Hz, which are close to the simulated values.
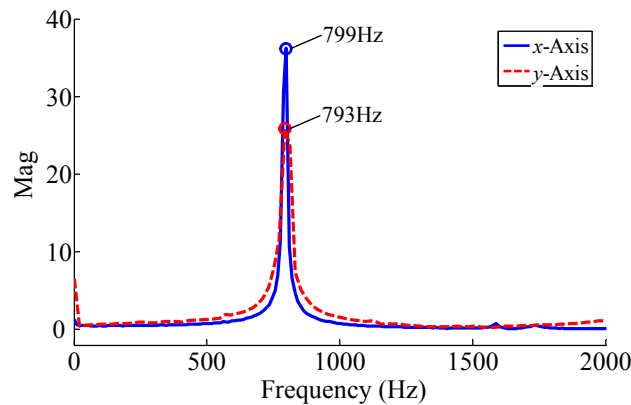
Figure 24. Natural frequency test of the CPM.

The step response of the CPM was tested where only the piezoelectric actuators adopted the closed-loop control. The result of the 1 μm step response test of the *x*-axis is shown in Figure 25. The rising time was 8 ms without overshoot. Similar results in the *y*-axis were obtained, but are not shown herein. The results show that the CPM has a rapid response performance.
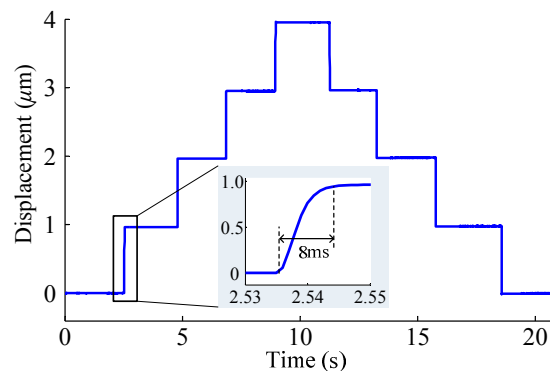
Figure 25. Step response test of the *x*-axis of the stage.

The positioning resolution of the CPM was tested in the closed-loop control. A consecutive-step positioning with a step size of 2 nm was carried out for each axis; results are shown in Figure 26. The steps can be clearly identified, which indicates that the positioning resolution of the CPM is better than 2 nm. Moreover, the resolution can be improved by filtering the measurement noise.

The output decoupling performance of the 2-DOF CPM was evaluated by actuating one axis and measuring the displacement output of the terminal platform along the other axis. The CPM's maximum output motion ranges along the two axes were both set as 40 μm. Figure 27 shows the coupled motions along the two axes when the preload force along the *x*-axis changed from 240 N to 320 N while the preload force along the *y*-axis remained unchanged. It can be seen that the coupling motions along the *y*-axis varied significantly as the preload force changed. However, the variation of the coupling motions along the *x*-axis was slight.
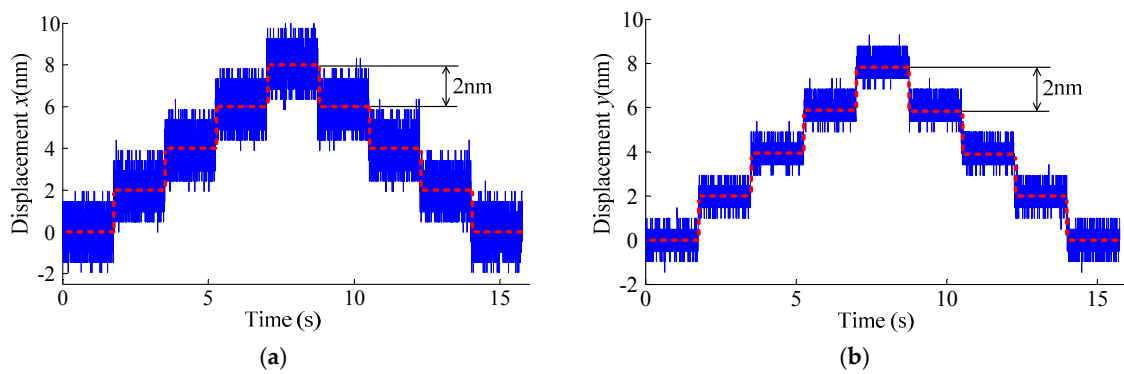
Figure 26. Positioning resolution test of the stage. (**a**) Positioning resolution of the *x*-axis. (**b**) Positioning resolution of the *y*-axis.
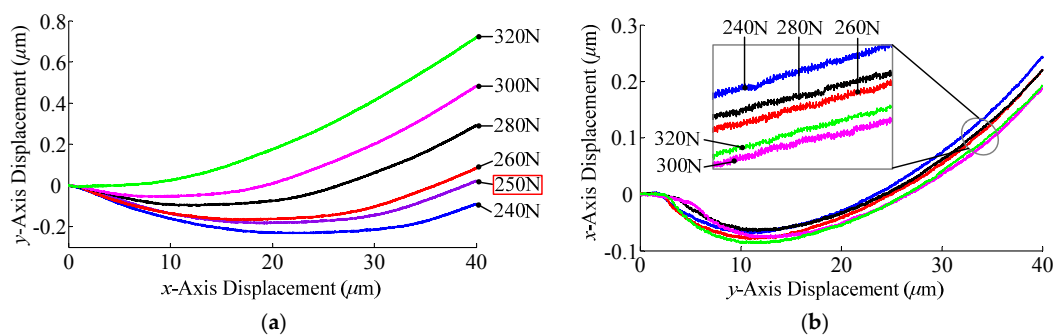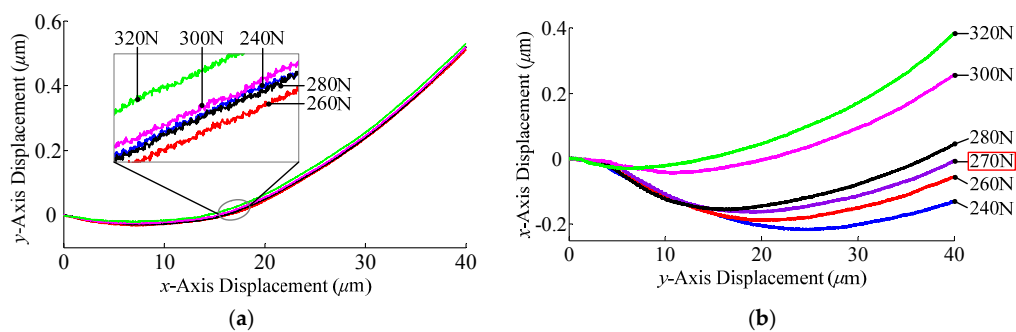

Figure 27. Coupling motions along the two axes when the preload force along the *x*-axis changes. (**a**) Coupling motion along the *x*-axis. (**b**) Coupling motion along the *y*-axis.

The coupling motions along the two axes when the preload force along the *y*-axis changed from 240 N to 320 N are shown in Figure 28, and a similar conclusion can be obtained.

Figure 28. Coupling motions along the two axes when the preload force along the *y*-axis changes. (**a**) Coupling motion along the *x*-axis. (**b**) Coupling motion along the *y*-axis.

The cases shown in Figures 27 and 28 may come from manufacturing errors in the flatness of the measuring datum planes. Figure 29 provides an explanation for the tested results of the coupling motions when the preload force along the *x*-axis changes. It can be seen that the variation of the preload load force along the *x*-axis will alter the initial measuring point on the terminal platform while testing the coupling motions along the *y*-axis. The initial measuring point, however, remains the same when testing the coupling motions along the *x*-axis. Therefore, the flatness of the measuring datum planes will influence the test of the coupling motions along the *y*-axis when the preload force along the *x*-axis varies.
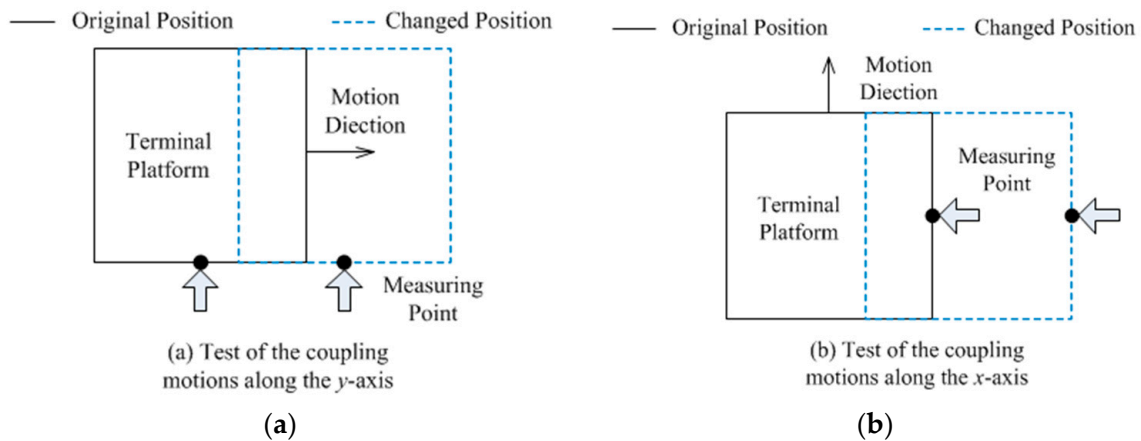
Figure 29. Coupling motion tests when the preload force along the *x*-axis changes. (**a**) Coupling motion along the *y*-axis. (**b**) Coupling motion along the *x*-axis.

Because the preload forces affect the coupling motions of the CPM, we can adjust the preload forces to minimize the cross-axis outputs. Through trial and error, the preload forces along the *x*- and *y*-axes, respectively, were chosen as 250 N and 270 N. The test for the two axes' output coupling was performed and the results are shown in Figure 30. It can be seen that the maximum output couplings between the two axes are less than 0.5%.
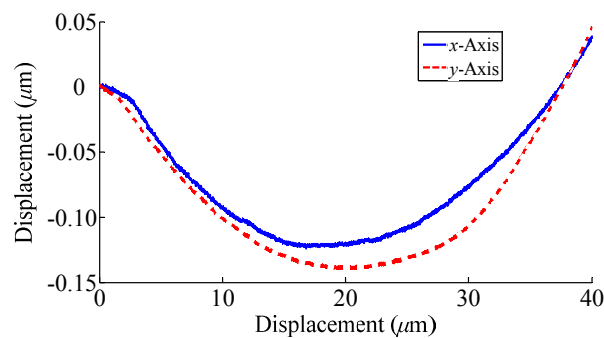

Figure 30. Output coupling evaluation of CPM through adjusting the preload forces.

Since the flatness of the measuring datum planes has a negative effect on the output decoupling performance of the CPM, the direct way of reducing its output coupling is to improve the manufacturing accuracy of the measuring base. The flatness of the measuring datum planes was improved to 1 μm. The preload forces along the two axes were set to 300 N. Then the output coupling of the CPM was re-evaluated and the results are given in Figure 31. It shows that the cross-axis outputs of the CPM are significantly reduced and the maximum output couplings between the two axes are only 0.105% and 0.045%, respectively.

The actuation point deformation should be measured to evaluate the ICD of the CPM, which is impossible to be achieved experimentally in this prototype. To conquer this problem, we proposed utilizing the ratio of the axial deformations at the two actuation points to reflect the input coupling performance of the 2-DOF CPM. Because of the linear displacement–force relation as shown in Figure 22, the changes of axial forces along the two axes were detected to indirectly evaluate the input coupling of the CPM. Tests were run on the variations of axial forces along the two axes when the *x*- or *y*-axis is actuated, shown in Figure 32. The results show that when the CPM moves through the whole range along the *x*-axis, the changes of the axial forces along the *x*- and *y*-axes are 169.4 N and 0.41 N, respectively. When the CPM moves through the whole range along the *x*-axis, the changes of the axial forces along the *x*- and *y*-axes are 0.34 N and 170.2 N, respectively. The corresponding coupling ratios

can be calculated as 0.24% and 0.20%, where the theoretical values calculated by Equation (28) are all 0.084%. The difference may lie in manufacturing and assembling errors. Regardless, this method provides a feasible way to evaluate the input coupling of the CPM and demonstrates this prototype's excellent input decoupling performance.
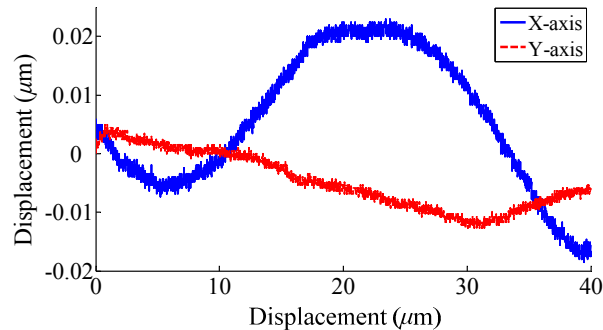

Figure 31. Output coupling evaluation of CPM through improving the manufacturing accuracy of the measuring datum.
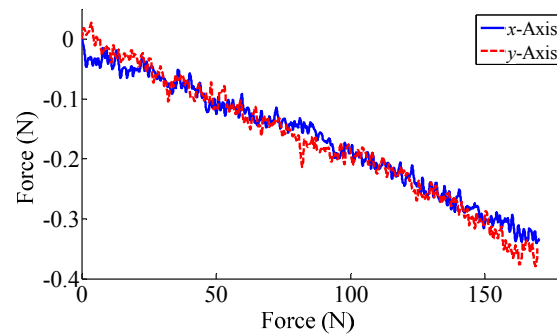

Figure 32. Input coupling evaluation of CPM.

This study also evaluated the contour tracking of the CPM for 2-D trajectories, to reflect the two-axis cooperative tracking performance. To adequately verify the decoupling performances of the CPM, the actuators in the CPM were controlled independently without any additional kinematic calibration or compensation. A Proportion-Integration algorithm was utilized to realize the closed-loop control.

The 2-D tracking results for $30°$, $45°$, and $60°$ lines with a contouring velocity of 40 µm/s are shown in Figure 33a, and the corresponding contouring errors have been plotted in Figure 33b. The contouring error here is defined as the minimum distance between the actual position and desired trajectory along an orthogonal direction to the trajectory. The results show that the maximum contouring error is smaller than 25 nm.

The experimental tests of circular contouring at different frequencies are shown in Figure 34, where the radius of the circles is 10 µm. The measured circular trajectories are coincident with the ideal trajectory without elliptical distortion, which contributes to the identical dynamic characteristics and excellent decoupling performance of the two axes. To obtain a more intuitive comparison, the maximum and average contouring errors of the circular contour with different frequencies has been illustrated in Figure 35. The results show that the contouring errors grow up as the frequency increases, and the maximum error is less than 150 nm. The contouring accuracy can be improved with the help of an advanced control strategy, which will be investigated in our future work.
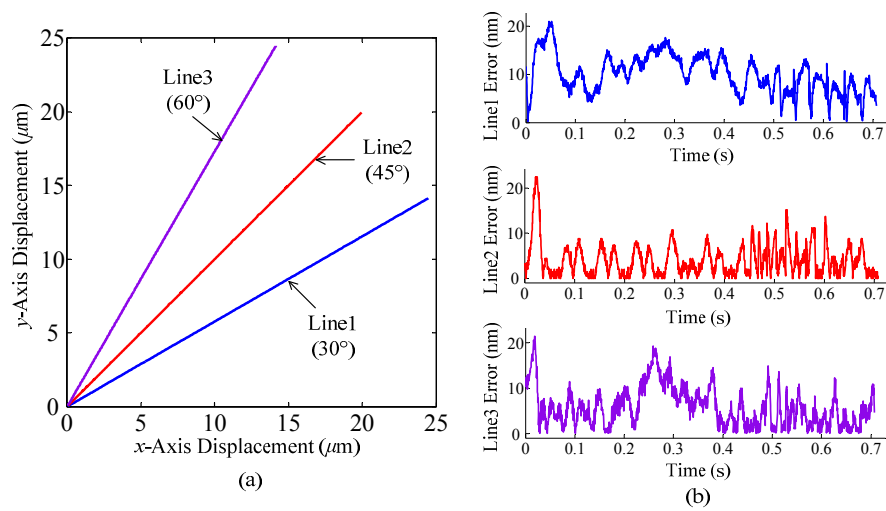
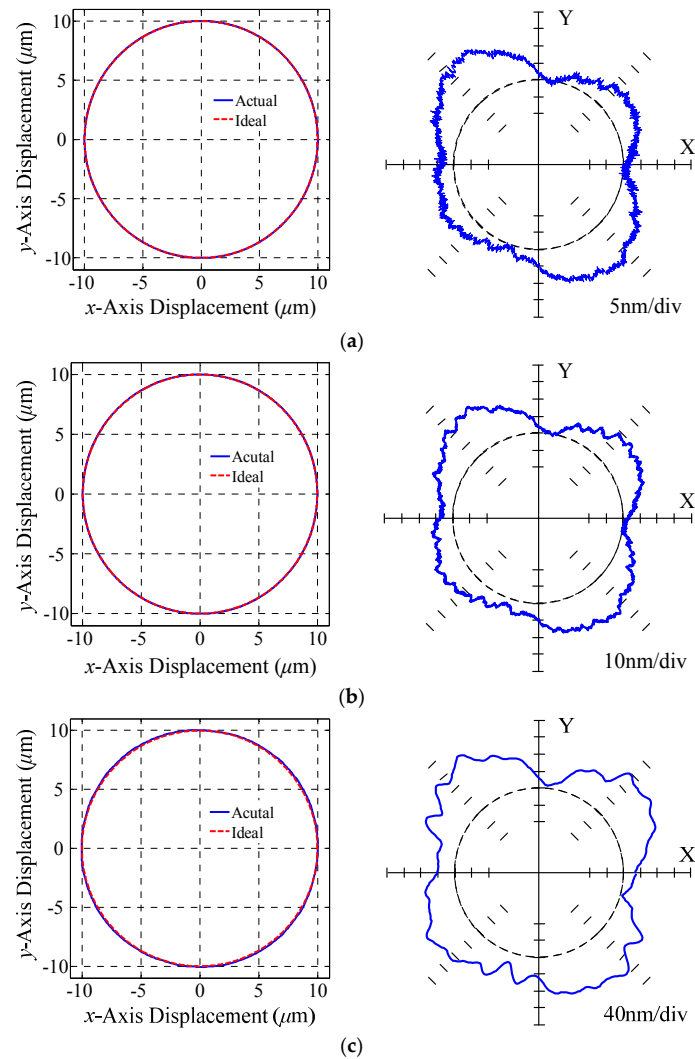**Figure 33.** Experimental results of 2-D linear contouring: (**a**) linear contours; and (**b**) contour accuracy.

Figure 34. Circular contouring performance at different frequencies: (**a**) f = 0.5 Hz; (**b**) f = 1 Hz; and (**c**) f = 5 Hz.
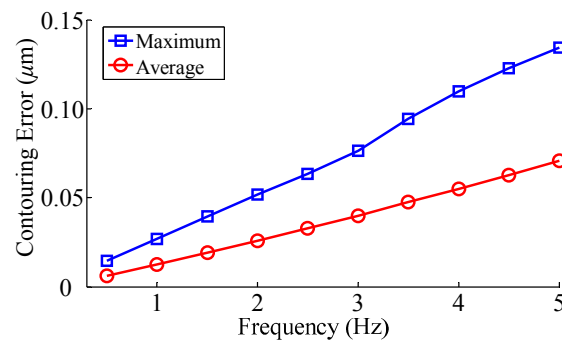
Figure 35. Circular contouring errors versus frequency.

6. Conclusions

A systematic design method of a 2-DOF CPM with excellent input and output decoupling performances was presented in this paper. The symmetric kinematic structure of the CPM can ensure the mechanism with a total output decoupling character. The input coupling was reduced by resorting to a flexure-based decoupler and geometric parameter optimization. The ICD of the optimized mechanism calculated using the analytical model was as low as 0.279%. A prototype was fabricated according to the optimized result with a measured workspace of 45.21 μm × 45.63 μm; the first two natural frequencies were 793 Hz and 799 Hz. The consecutive-step tests showed that this stage has a high resolution that was better than 2 nm and the rising time of 1 μm step test was only 8 ms without overshoot. The cross-axis outputs of the CPM were minimized by adjusting the preload forces and improving the manufacturing accuracy of the measuring base, and the maximum output coupling between the two axes was only about 0.1%. The input coupling was indirectly evaluated by detecting the axial force variations along the two axes and the coupling ratios were 0.24% and 0.20%. Moreover, the experimental studies show that high tracking accuracy was obtained in the biaxial linear and circular contouring tests, in which the two actuators were controlled independently without any additional kinematic calibration or compensation. Considering they performed well, the developed CPM can be suitable for applications in which high precision and resolution are needed, such as the atomic force scanner and biological manipulation; this will be the goal of our future work.

Author Contributions: Yao Jiang and Tiemin Li proposed the design idea; Yao Jiang performed the design method and developed the prototype of the 2-DOF compliant parallel mechanism; Liping Wang and Feifan Chen performed the experiments and analyzed the data; and Tiemin Li and Yao Jiang wrote the paper together.

Conflicts of Interest: The authors declare no conflict of interest.

References

1. Schitter, G.; Thurner, P.; Hansma, P. Design and input-shaping control of a novel scanner for high-speed atomic force microscopy. *Mechatronics* **2006**, *18*, 282–288. [CrossRef]
2. Arai, S.; Wilson, S.; Corbett, J.; Whatmore, R. Ultra-precision grinding of PZT ceramics—Surface integrity control and tooling design. *Int. J. Mach. Tools Manuf.* **2009**, *49*, 998–1007. [CrossRef]
3. Ramadan, A.; Takubo, T.; Mae, Y.; Oohara, K.; Arai, T. Development process of a chopstick-like hybrid-structure two-fingered micromanipulator hand for 3-D manipulation of microscopic objects. *IEEE Trans. Ind. Electron.* **2009**, *56*, 1121–1135. [CrossRef]
4. Li, T.; Zhang, J.; Jiang, Y. Derivation of empirical compliance equations for circular flexure hinge considering the effect of stress concentration. *Int. J. Precis. Eng. Manuf.* **2005**, *16*, 1735–1743. [CrossRef]
5. Yue, Y.; Gao, F.; Zhao, X.; Ge, Q. Relationship among input-force, payload, stiffness and displacement of a 3-DOF perpendicular parallel micro-manipulator. *Mech. Mach. Theory* **2010**, *45*, 756–771. [CrossRef]

6. Choi, K.; Kim, D. Monolithic parallel linear compliant mechanism for two axes ultraprecision linear motion. *Rev. Sci. Instrum.* **2006**, *77*, 065106. [CrossRef]

7. Li, Y.; Xu, Q. A novel piezoactuated XY stage with parallel decoupled, and stacked flexure structure for micro-/nanopositioning. *IEEE Trans. Ind. Electron.* **2011**, *58*, 3601–3615. [CrossRef]

8. Kenton, B.; Leang, K. Design and control of a three-axis serial-kinematic high-bandwidth nanopositioner. *IEEE Trans Mechantron.* **2012**, *17*, 356–369. [CrossRef]

9. Yao, Q.; Dong, J.; Ferreira, P. Design, analysis, fabrication and testing of a parallel-kinematic micropositioning XY stage. *Int. J. Mach. Tools Manuf.* **2007**, *47*, 946–961. [CrossRef]

10. Jiang, Y.; Li, T.; Wang, L. The dynamic modeling, redundant-force optimization and dynamic performance analyses of a parallel kinematic machine with actuation redundancy. *Robotica* **2015**, *33*, 241–263. [CrossRef]

11. Jiang, Y.; Li, T.; Wang, L. Dynamic modeling and redundancy force optimization of a 2-DOF parallel kinematic machine with kinematic redundancy. *Robot. Comput. Integr. Manuf.* **2015**, *32*, 1–10. [CrossRef]

12. Poilt, S.; Dong, J. Development of a high-bandwidth XY nanopositioning stage for high-rate micro-nanomanufacturing. *IEEE Trans. Mechatron.* **2011**, *16*, 724–733. [CrossRef]

13. Liang, Q.; Zhang, D.; Chi, Z.; Song, Q.; Ge, Y.J.; Ge, Y. Six-DOF micro-manipulator based on compliant parallel mechanism with integrated force sensor. *Robot. Comput. Integr. Manuf.* **2011**, *27*, 124–134. [CrossRef]

14. Xiao, S.; Li, Y. Development of a large working range flexure- based 3-DOF micro-parallel manipulator driven by Electromagnetic Actuators. In Proceedings of the IEEE International Conference on Robotics and Automation, Karlsruhe, Germany, 6–10 May 2013; pp. 4506–4511.

15. Jia, X.; Liu, J.; Tian, Y.; Zhang, D. Stiffness analysis of a compliant precision positioning stage. *Robotica* **2012**, *30*, 925–939. [CrossRef]

16. Awtar, S.; Slocum, A. Design of parallel kinematic XY flexure mechanisms. In Proceedings of the International Design Engineering Technical Conferences & Computer and Information in Engineering Conference, Long Beach, CA, USA, 24–28 September 2005; pp. 89–99.

17. Li, Y.; Xu, Q. Design of a new decoupled XY flexure parallel kinematic manipulator with actuator isolation. In Proceedings of the IEEE/RSJ International Conference on Intelligent Robots and Systems, Nice, France, 22–26 September 2008; pp. 470–475.

18. Hao, G.; Yu, J. Design, modeling and analysis of a completely-decoupled XY compliant parallel manipulator. *Mech. Mach. Theory* **2016**, *102*, 179–195. [CrossRef]

19. Awtar, S.; Slocum, A. Constraint-based design of parallel kinematic XY flexure mechanisms. *J. Mech. Des.* **2007**, *129*, 816–830. [CrossRef]

20. Lai, L.; Gu, G.; Zhu, L. Design and control of a decoupled two degree of freedom translational parallel micro-positioning stage. *Rev. Sci. Instrum.* **2012**, *83*, 045105. [CrossRef] [PubMed]

21. Qin, Y.; Shirinzadeh, B.; Tian, Y.; Zhang, D.; Bhagat, U. Design and computational optimization of a decoupled 2-DOF monolithic mechanism. *IEEE Trans. Mechatron.* **2014**, *19*, 872–881. [CrossRef]

22. Li, Y.; Xu, Q. Development and assessment of a novel decoupled XY parallel micropositioning platform. *IEEE Trans. Mechatron.* **2010**, *15*, 125–135.

23. Li, C.; Gu, G.; Yang, M.; Zhu, L. Design, analysis and testing of a parallel-kinematic high-bandwidth XY nanopositioning stage. *Rev. Sci. Instrum.* **2013**, *84*, 125111. [CrossRef] [PubMed]

24. Blanding, D. *Exact Constraint: Machine Design Using Kinematic Principle*; ASME Press: New York, NY, USA, 1999.

25. Hopkins, J.; Culpepper, M. Synthesis of multi-degree of freedom, parallel flexure system concepts via freedom and constraint topology (FACT). Part I: Principles. *Precis. Eng.* **2010**, *34*, 259–270. [CrossRef]

26. Hopkins, J.; Culpepper, M. Synthesis of multi-degree of freedom, parallel flexure system concepts via freedom and constraint topology (FACT). Part II: Practice. *Precis. Eng.* **2010**, *34*, 271–278. [CrossRef]

27. Yong, Y.; Aphale, S.; Moheimani, S. Design, identification, and control of a flexure-based XY stage for fast nanoscale positioning. *IEEE Trans. Nanotechnol.* **2009**, *8*, 46–54. [CrossRef]

28. Schitter, G.; Astrom, K.; DeMartini, B.; Thurner, P.; Turner, K.; Hansma, P. Design and modeling of a high-speed AFM-scanner. *IEEE Trans. Control Syst. Technol.* **2007**, *15*, 906–915. [CrossRef]

29. Tang, H.; Li, Y. Design, analysis, and test of a novel 2-DOF nanopositioning system driven by dual mode. *IEEE Trans. Robot.* **2014**, *29*, 650–662. [CrossRef]

30. Hao, G.; Kong, X. A novel large-range XY compliant parallel manipulator with enhanced out-of-plane stiffness. *J. Mech. Des.* **2012**, *134*, 061009. [CrossRef]

31. Jiang, Y.; Li, T.; Wang, L. Stiffness modeling of compliant parallel mechanisms and applications in the performance analysis of a decoupled parallel compliant stage. *Rev. Sci. Instrum.* **2015**, *86*, 095109. [CrossRef] [PubMed]

32. Shieh, H.; Hsu, C. An adaptive approximator-based backstepping control approach for piezoactuator- driven stages. *IEEE Trans. Ind. Electron.* **2008**, *55*, 1729–1738. [CrossRef]

33. Xu, Q. Design and development of a compact flexure-based XY precision positioning system with centimeter range. *IEEE Trans. Ind. Electron.* **2014**, *61*, 893–903. [CrossRef]

34. Vallance, R.; Haghighian, B.; Marsh, E. A unified geometric model for designing elastic pivots. *Precis. Eng.* **2008**, *32*, 278–288. [CrossRef]

35. Dirksen, F.; Lammering, R. On mechanical properties of planar flexure hinges of compliant mechanisms. *Mech. Sci.* **2011**, *2*, 109–117. [CrossRef]

36. Koseki, Y.; Tanikawa, T.; Koyachi, N.; Arai, T. Kinematic analysis of a translational 3-DOF micro-parallel mechanism using the matrix method. *Adv. Robot.* **2002**, *16*, 251–264. [CrossRef]

37. Pham, H.H.; Chen, I.M. Stiffness modeling of flexure parallel mechanism. *Precis. Eng.* **2005**, *29*, 467–478. [CrossRef]